photonics

MDPI

Article

Extended Coherent Modulation Imaging for Object Reconstruction with Single Diffraction Pattern

Yue Wang, Yafang Zou, Ye Wu, Xinke Li, Xibao Gao, Long Jin, Weiyou Zeng, Qinglan Wang and Xi He *

Shiyan Key Laboratory of Quantum Information and Precision Optics, Collaborative Innovation Center for Optoelectronic Technology of Ministry of Education and Hubei Province, and School of Optoelectronic Engineering, Hubei University of Automotive Technology, Shiyan 442002, China; 202208123@huat.edu.cn (Y.W.); 202208124@huat.edu.cn (Y.Z.); 202208186@huat.edu.cn (Y.W.); 20210064@huat.edu.cn (X.L.); xibaogao@huat.edu.cn (X.G.); 20140007@huat.edu.cn (L.J.); zengwy_lx@huat.edu.cn (W.Z.); wangql_lx@huat.edu.cn (Q.W.)

* Correspondence: hexi2014010@outlook.com

Abstract

Coherent diffraction imaging (CDI) is a fast-growing imaging technique. Among all CDI methods, coherent modulation imaging (CMI) has strong potential for dynamic imaging because of its ability to form an image from a single diffraction pattern. However, current CMI methods mostly reconstruct the exit wave distribution behind the object plane, which is seriously affected by the illumination artifact. Recently, some improved CMI methods have been developed to resolve the problem. However, many of these methods still need two diffraction patterns—one empty-sample diffraction pattern and another snapshot measurement. Recent advances in randomized probe imaging have shown that a single diffraction pattern suffices for quantitative reconstruction when the probe is pre-calibrated. Herein, we propose a modified CMI algorithm to reconstruct pure object function with single diffraction pattern, thereby simplifying the experimental process. Moreover, the proposed method can also work in the situation where the modulation effect is weak. Both numerical simulations and optical experiments have been conducted to verify the proposed method.

Keywords: coherent modulation imaging; phase retrieval; object function; single diffraction pattern

1. Introduction

As a lens-free phase imaging method, coherent diffraction imaging (CDI) [1–3] can reconstruct the complex transmittance of a target by utilizing the far-field diffraction pattern and an iterative algorithm. CDI has been widely used in fields that require high-contrast imaging and wavefront detecting [4–6] because of its simple scheme and the ability to achieve diffraction-limited resolution, especially in the fields of X-ray [7–13] and electron beam [14–16]. However, conventional CDI algorithms encounter the problems of stagnation and uniqueness of the solutions [17,18], and they are not well suited for extended sample imaging. Conventional ptychography [19–23] is an improved version of CDI that can reconstruct the complex amplitude of extended samples with fast convergence and strong robustness. However, it typically requires a large number of diffraction patterns; the associated long data-acquisition time makes it unsuitable for dynamic imaging scenarios that demand single-shot measurements. To address this limitation, single-shot ptychography has been developed [24,25], but this imaging method is affected by the

Check for updates

Received: 24 February 2026
Revised: 29 March 2026
Accepted: 31 March 2026
Published: 7 April 2026

Copyright: © 2026 by the authors. Licensee MDPI, Basel, Switzerland. This article is an open access article distributed under the terms and conditions of the Creative Commons Attribution (CC BY) license.

interference between adjacent diffraction patterns. As a recently developed CDI method, coherent modulation imaging (CMI) [26,27] introduces a phase modulator in front of the detector. Since the strong modulation effect enhances the differences between the true distribution and reconstructed distribution of incident beam at the modulator plane, the tolerance of wavefront reconstruction error can be decreased [28], the convergence rate can be increased, and the ambiguities associated with plane-wave CDI can be eliminated. CMI can realize phase imaging with just one single diffraction pattern; it has been applied in the fields of optical metrology [29,30], dynamic imaging [31–33], biological imaging [27,34], wavefront detecting [35], and 3D imaging [36]. In addition, a variety of optimized algorithms [37–41] and imaging systems [42] regarding CMI have been proposed to improve the imaging quality.

Current CMI methods mostly reconstruct the exit wave function behind the object plane. However, there remains a possibility that the reconstruction results are affected by the illumination artifact. Fresnel CDI [43] can retrieve the object function under the premise that the illumination wave is known, but it is only effective for highly curved spherical illumination. The extended CMI (eCMI) method can retrieve the illumination and object function simultaneously [40], but it still needs two diffraction patterns—one empty-sample diffraction pattern and another snapshot measurement of the object—and it can work only when the modulator has strong modulation effect. Recent advances in randomized probe imaging (RPI) [44–46] can realize the quantitative object function reconstruction with single diffraction pattern; at a wavelength of 532 nm, the imaging resolution of RPI method can reach 31 μm. Kang [47] proposed a single-frame CDI method using a triangular aperture that can reconstruct the object function from a single diffraction pattern. However, in this method, the diffraction pattern needs to be generated from Fraunhofer diffraction and it is not possible to place the object plane flexibly, that is, this method can efficiently work only when the shape of the aperture is not point symmetrical and the object plane is close to the aperture plane.

In this work, we aim to improve the current CMI method so that it can reconstruct the pure object function from just a single diffraction pattern and the object axial location can be changed flexibly. On the basis of CMI optical path, a modified phase retrieval algorithm (extended CMI with single diffraction pattern) is proposed. The algorithm has been verified both in simulation and experiment. The results show that not only the pure object function, free from illumination artifact, can be reconstructed, but this method can also work when the modulation effect is weak.

2. Principle of the Extended CMI with Single Diffraction Pattern

The optical path of the extended CMI with a single diffraction pattern is shown in Figure 1.

This basic experimental setup consists of a detector, a random phase plate as a wavefront modulator, a sample, and an aperture. The shape of explicitly defined aperture could be circular or triangular—both shapes are feasible in simulation and experiment (results shown later). The wavefront incident on the aperture plane is a plane wave, the distance of the object plane from the aperture plane and that from the modulator plane are d_1 and d_2, respectively, and the distance between the modulator plane and detector plane is L. The complex amplitude distribution of modulator is known as M. When the sample is placed in the setup, one snapshot is taken by CCD detector. The recorded diffraction pattern I is then fed into the modified reconstruction algorithm for pure object function retrieval.

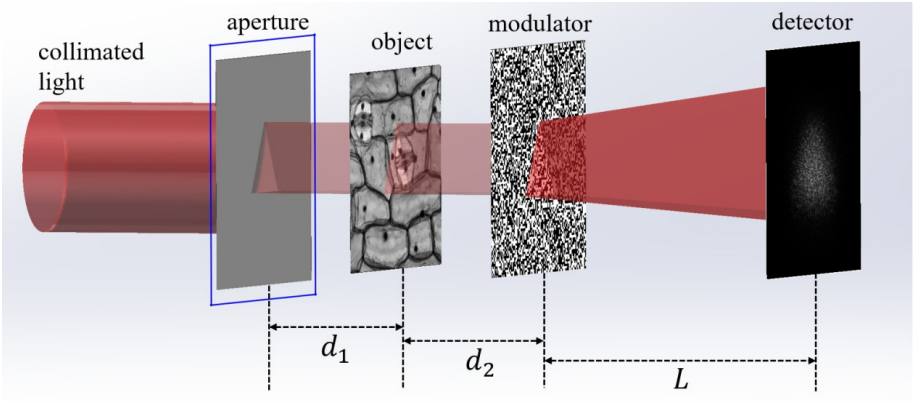


Figure 1. Optical path of the extended CMI with a single diffraction pattern. In the experiment, A CMOS detector (Allied Vision Mako G-419B, Germany) is used. The modulator is mounted on a X-Y translation stage (Thorlabs M-Z9, USA) The aperture shape can be circular or triangular. The wavelength of the collimated light is 632.8 nm before the single exposure of the detector. The distribution of the modulator is measured by ptychography. The computational setup is a Dell workstation equipped with an NVIDIA RTX A4000 GPU (made in USA).

The reconstruction algorithm starts from the aperture plane with an estimate of the aperture exit wave ψ_k. Since the incident wave is a plane wave, ψ_k should be the transmission function of the explicitly defined aperture. The k-th iteration process is described as follows:

(1) The illumination probe distribution P_k over the distance d_1 to the object plane is calculated using angular spectrum propagation method.

$$P_k = \mathcal{F}\{\psi_k, d_1\} \tag{1}$$

where $\mathcal{F}\{\}$ represents the free-space wave propagator.

(2) The illumination probe function is multiplied by the object estimate O_k, which generates the object exit wave.

$$\varphi_k = P_k O_k \tag{2}$$

(3) φ_k is propagated to the modulator plane to form the modulator incident wave $g_k = \mathcal{F}\{\varphi_k, d_2\}$. This incident wave is then modulated by multiplying the modulator function M, generating the modulator exit wave.

$$h_k = g_k M \tag{3}$$

(4) h_k is propagated to the detector plane to form the diffraction pattern D_k.

$$D_k = \mathcal{F}\{h_k, L\} \tag{4}$$

(5) By replacing modulus of D_k with $\sqrt{I}$, keeping the phase of D_k unchanged, the updated diffraction pattern D'_k at the detector plane is obtained.

$$D'_k = \sqrt{I} \cdot \frac{D_k}{|D_k|} \tag{5}$$

(6) The revised diffraction pattern D'_k is propagated back to the modulator plane to form an updated modulator exit wave $h'_k = \mathcal{F}^{-1}\{D'_k, L\}$. Then the modulation effect is undone according to Equation (6).

$$g'_k = g_k + \alpha_1 \frac{M^*|M|}{\left(|M|^2 + \beta_1\right)|M|_{max}}(h'_k - h_k) \tag{6}$$

where α_1 and β_1 are constants for updating; in this algorithm α_1 and β_1 are set to be 1.

(7) The updated wave field g'_k is propagated back to the object plane and the updated object exit wave φ'_k is obtained, where $\varphi'_k = \mathcal{F}^{-1}\{g'_k, d_2\}$. Then, the object function and the illumination probe are updated using the following equations:

$$O'_k = O_k + \alpha_2 \frac{P_k^*}{|P_k|^2_{max}}(\varphi'_k - \varphi_k) \tag{7}$$

$$P'_k = P_k + \alpha_3 \frac{O_k^*}{|O_k|^2_{max}}(\varphi'_k - \varphi_k) \tag{8}$$

where α_2 and α_3 are weight coefficients for the k-th iteration; α_2 and α_3 can take values within [0,1]. In this work, α_2 and α_3 are set to 0.2 and 0.8, respectively.

(8) The updated probe function P'_k is propagated back to the aperture plane to obtain the exit wave of aperture, $\psi'_k = \mathcal{F}^{-1}\{P'_k, d_1\}$. The wavefield behind the aperture is then updated according to Equation (9).

$$\psi_{k+1} = \begin{cases} \frac{1}{N}\sum_r |\psi'_k(r)|, & (r \in S \wedge |\psi'_k(r)| \geq 0), \\ 0, & otherwise \end{cases} \tag{9}$$

where S represents the range of the aperture, r represents the real-space coordinate vector, and N denotes the number of r that satisfies the condition in Equation (9).

(9) The steps 1–8 are repeated till a specified termination criterion is met and the output of the proposed algorithm is a pure object function. The reconstructed quality is evaluated by calculating the Fourier ring correlation (FRC),

$$FRC = \frac{\sum Re\{F \cdot G^*\}}{\sqrt{\left(\sum |F|^2\right) \cdot \left(\sum |G|^2\right)}} \tag{10}$$

where F and G are the Fourier transforms of the reconstructed pure object function and the original object function, respectively.

Notice that this proposed algorithm is similar to the eCMI algorithm; however, a key distinction lies in the illumination probe update strategy at the aperture plane, which is governed by Equation (9)—the same formulation adopted in Reference [47]. Equation (9) updates the probe function from an explicitly defined aperture, thereby yielding a known, idealized plane-wave function, Consequently, probe initialization and updating can be performed analytically—without requiring a second diffraction measurement. While this update strategy may be effective in numerical simulation, experimental implementation faces inherent limitations: perfect plane-wave illumination is unattainable due to optical aberrations, beam non-uniformity, and alignment imperfections. As a result, minor artifacts may appear in the reconstructed images; however, quantitative evaluation confirms that these deviations remain localized and exert negligible influence on the overall structural fidelity and quantitative accuracy of the reconstruction.

Reference [47] employs Equation (9) to update the probe function. In the simulations reported therein, triangular apertures yield higher reconstruction quality than circular ones. This improvement arises because Equation (9) implements a support-free update strategy—i.e., it does not explicitly enforce a support constraint—and thus relies implicitly

on the physical aperture shape to provide structural guidance for convergence. According to Reference [48], phase retrieval algorithm may converge more readily to the desired solution when it has non-centrosymmetrical support, thus the reconstruction quality of non-centrosymmetrical apertures like triangle and pentagon are much better. In our proposed method, we retain the same probe update rule based on Equation (9), but augment it with an explicit modulator constraint. This constraint actively enforces physically consistent amplitude-phase relationships in the probe, thereby improving reconstruction quality independently of aperture geometry.

3. Numerical Simulation

To demonstrate the validity of the proposed method, numerical simulations were performed. Two pictures were selected as the amplitude and phase of the object, as shown in Figure 2a,b. The diameter of the circular aperture was 200 pixels. For comparison, another triangular aperture with same area was also used. The dashed circle and triangle indicate the main illuminated area. The random phase plate used in the simulation was a binary step phase plate with known randomly distributed binary phases of 0 or 3.14 radians (as shown in Figure 2c). The minimum feature size of the random phase plate was 11 μm, the pixel size and resolution of the detector were 5.5×5.5 μm^2 and 1024×1024, respectively. Poisson noise was added to the diffraction pattern intensities. The wavelength of the coherent light source was 632.8 nm. The distance between the phase plate and the detector was 20 mm, and the distance between the aperture plane and the phase plate was 30 mm.

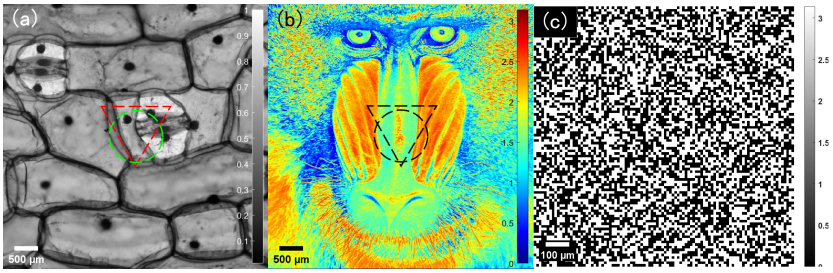


Figure 2. The amplitude (**a**) and phase (**b**) of original object; (**c**) the phase distribution of the random phase plate; the dashed circle and triangle indicate the main illuminated area.

First, the complex-valued object placed at aperture plane was tested ($d_1 = 0$ mm). As the plane wave illuminated the aperture and the detector took a single shot of the object measurement, the intensity of the diffraction pattern and distribution of the phase plate were taken into the algorithm for 300 iterations; the reconstructed results are shown in Figure 3a,e. It can be seen that the pure object function is retrieved well regardless of whether the aperture is circular or triangular. The FRC plots in Figure 4a for both aperture shapes keep high values. Then, this object was placed at distances $d_1 = 10,\ 15,$ and 20 mm away from the aperture plane, with the corresponding distances $d_2 = 20,\ 15,$ and 10 mm, respectively. The reconstructed results are shown in Figure 3, and the corresponding FRC plots are shown in Figure 4a. The results indicate that reconstructed image quality gradually deteriorates as the distance d_1 increases. This degradation stems from two interrelated effects: first, the illumination area at the modulator plane shrinks with increasing d_1, thereby weakening the modulation effect; second, the probe boundary becomes increasingly blurred due to propagation-induced diffraction, which in turn leads to ill-defined boundaries in the illuminated object region. Nevertheless, the retrieved object function retains high fidelity, and the overall degradation remains modest.

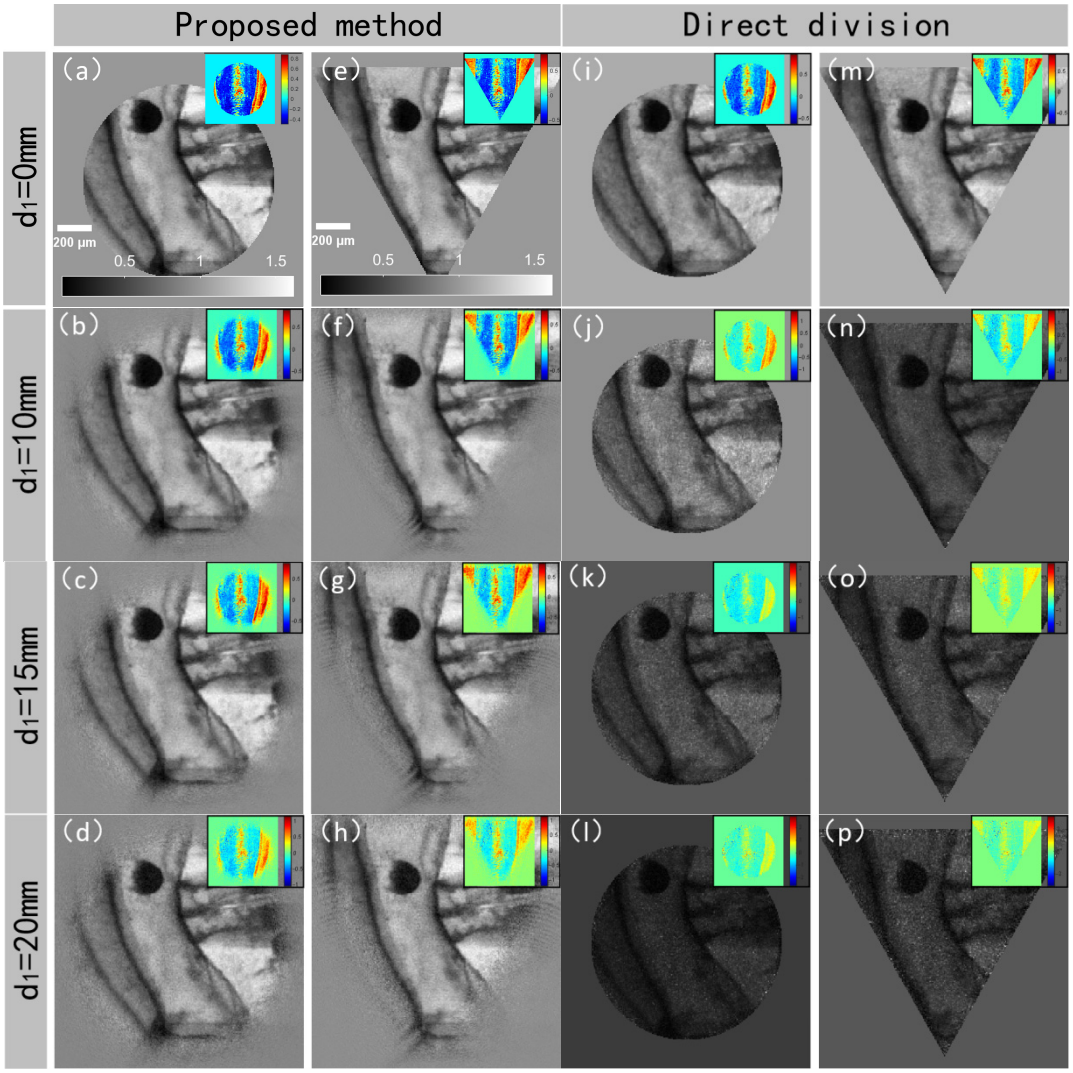


Figure 3. Simulated results. (**a**–**d**) The reconstructed amplitude and phase of pure object function at different distances by the proposed method with circular aperture. (**e**–**h**) The reconstructed amplitude and phase of pure object function at different distances by the proposed method with triangular aperture. (**i**–**l**) The reconstructed amplitude and phase of pure object function at different distances by direct divison method with circular aperture. (**m**–**p**) The reconstructed amplitude and phase of pure object function at different distances by direct division method with triangular aperture. The intsets in (**a**–**p**) are the reconstructed phase.

For comparative purposes, conventional CMI reconstructions across three planes were performed. The object transmission function was retrieved via direct division of the reconstructed exit wavefield by the reconstructed illumination probe at the object plane. Specifically, the exit wavefield and probe were independently reconstructed using conventional CMI; an amplitude threshold of 0.1 was applied to isolate the region of interest—only pixels with probe amplitude exceeding this threshold were retained. Subsequently, the object function was computed as the pixel-wise quotient of the exit wavefield and the probe, with a small regularization constant (0.01) added to the denominator to prevent numerical instability arising from near-zero probe amplitudes. The results in Figure 3i–p showed that only when the object and the aperture were at the same plane, the object function can be reconstructed roughly. When the object was at other distances, the reconstructed quality would be seriously degraded as the distance d_1 increased, as shown in Figure 4b.

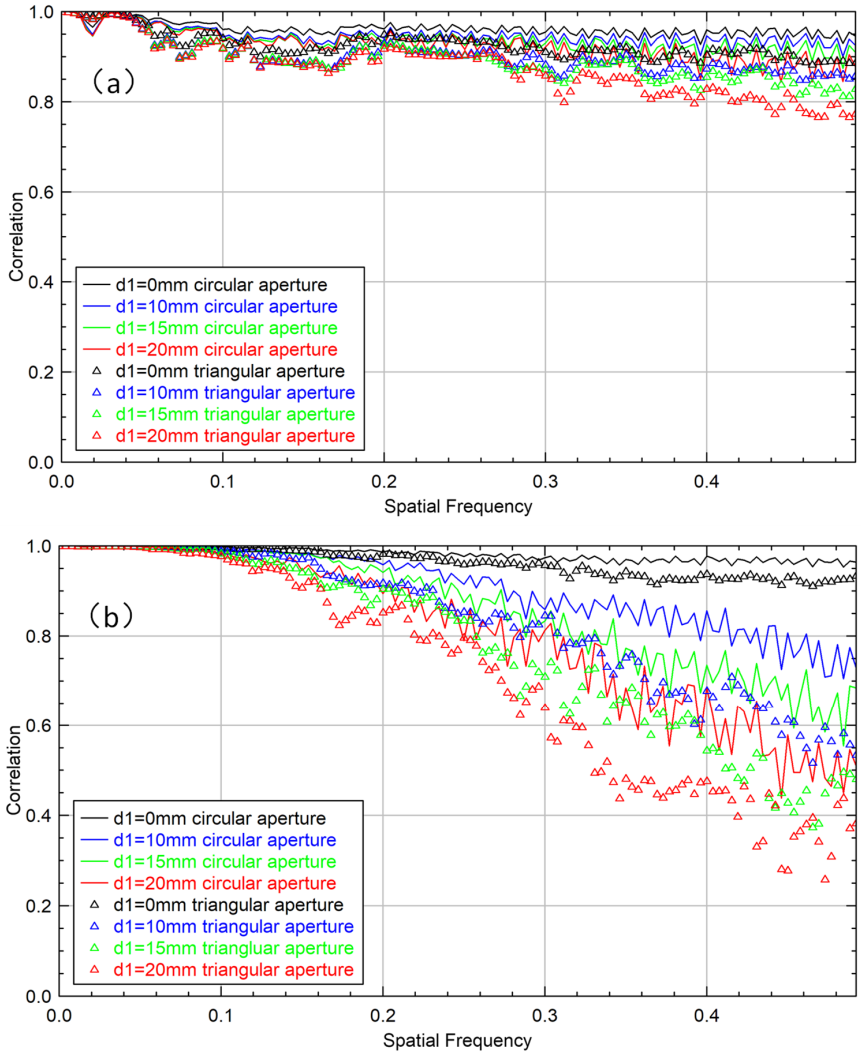


Figure 4. Fourier ring correlation plot of the reconstructed image. (**a**) The FRC plot obtained using the proposed method; (**b**) the FRC plot obtained using direct-division method.

In order to retrieve the best object function, the true value of d_1 needs to be known accurately. However, in practical experiment, the measured value of d_1 always has an error, and thus, an autofocus algorithm needs to be applied to find the true value. Here, we employed the method proposed in Reference [49]. The autofocus procedure consists of three steps. First, a series of wavefronts are obtained by propagating the roughly reconstructed object to a set of locations around the estimated d_1 with a small step size Δz. These wavefronts are properly cropped, and their amplitudes are retained for use. Then the normalized Tamura coefficient is calculated for each amplitude image. Since the location of the peak of the Tamura coefficient curve against the propagation distance dz indicates the correct object distance, the in-focus object function can be retrieved using this modified distance $d_1 + dz$. The process is shown in Figure 5.

The modulation effect of the modulator also influences the proposed method; thus, a simulation was conducted to investigate the relationship between the performance of the proposed algorithm and the parameters of the modulator. With the object distance $d_1 = 10$ mm unchanged, four kinds of binary phase modulators with different modulation depths were tested, with the phase values of these four phase plates set to be $0/\frac{\pi}{8}$, $0/\frac{\pi}{4}$, $0/\frac{\pi}{2}$, and $0/\pi$. The reconstructed results, shown in Figure 6, indicated that with a decrease in the phase value of the modulator, the diffraction pattern contained fewer speckles, and the modulation effect became weaker. When the phase value of modulator was $0/\frac{\pi}{8}$,

the reconstruction worsened and the reconstructed object amplitude and phase exhibited crosstalk phenomena; however, the reconstructed amplitude still had a distinct outline.

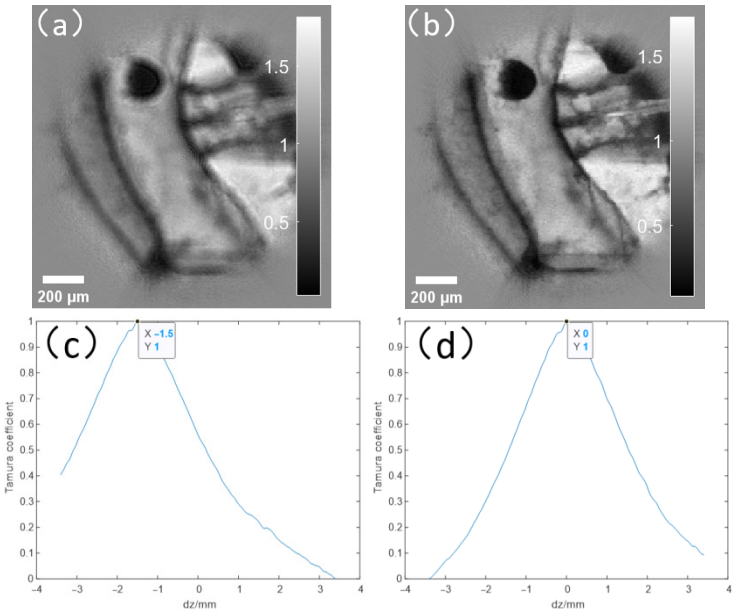


Figure 5. Process of autofocusing algorithm: the real value of d_1 was 10 mm, the measured value of d_1 was 11.5 mm, $\Delta z = 0.02$ mm, and $dz = -1.5$ mm. (**a**,**c**) are the reconstructed out-focus amplitude and the corresponding Tamura coefficient plot; (**b**,**d**) are the reconstructed in-focus amplitude and the corresponding Tamura coefficient plot.

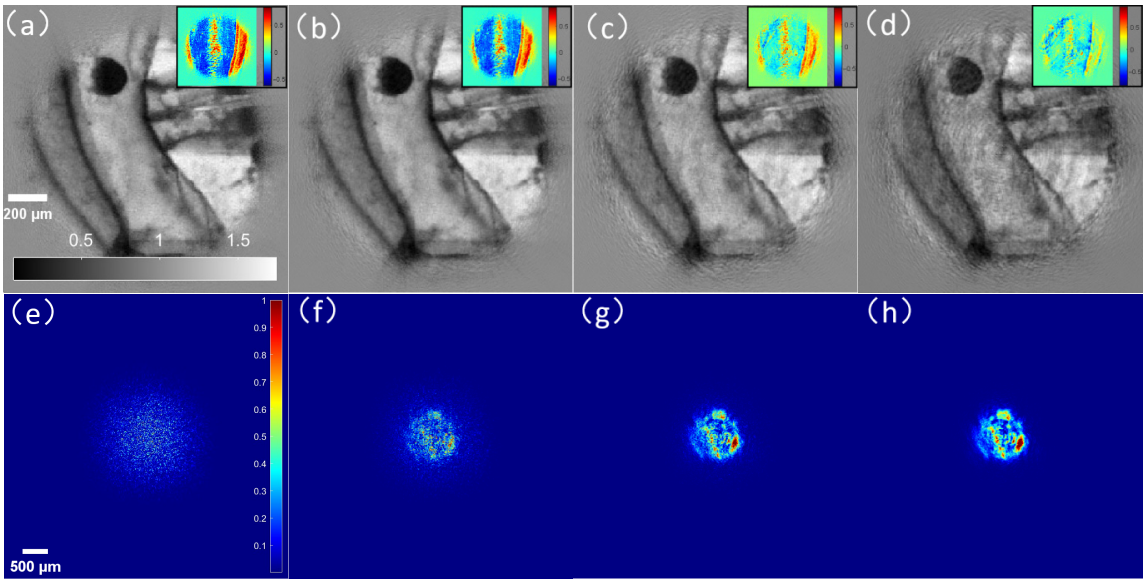


Figure 6. (**a**–**d**) The reconstruced amplitude and phase when the phase values of the modulator are $0/\pi$, $0/\frac{\pi}{2}$, $0/\frac{\pi}{4}$, $0/\frac{\pi}{8}$, respectively; (**e**–**h**) the corresponding diffraction patterns; the intsets in (**a**–**d**) are the reconstructed phase.

In actual experiments, the transmission function of the modulator is pre-characterized using ptychography; however, this measured transmission function inevitably contains errors. Such errors may arise from fabrication imperfections—particularly depth deviations during etching—as well as from limitations inherent to the ptychographic measurement itself. To quantitatively assess how these modulator-related errors affect the reconstruction fidelity of the proposed method, we conducted controlled simulations in which synthetic phase errors were introduced into the ground-truth modulator function. Specifically, we

added a uniformly distributed random phase perturbation over the interval [0, m] radians (with m = 0.5, 1.0, or 2.0) to the ideal modulator phase profile. Figure 7 shows both the erroneous modulator phase maps and the corresponding reconstructed complex function of measured object. As shown, when m = 0.5, reconstruction quality degrades only marginally: amplitude and phase features remain well preserved. At m = 1.0, degradation becomes moderate—the overall structural outline of both amplitude and phase remains discernible, albeit with increased speckle noise. When m = 2.0, reconstruction collapses entirely: neither amplitude nor phase exhibits recognizable spatial structure. The phase modulator employed in the actual experiment is a holographic diffuser plate, with a surface relief height of less than 0.5λ (where λ = 632.8 nm is the wavelength of light source). According to Reference [50], the mean square error of ptychography measurement could be stabilized at below 0.1, when the surface relief height of stepped sample is smaller than 1.5λ. Therefore, ptychography is expected to characterize the transmission function of the modulator with exceptional accuracy, thereby minimizing the propagation of calibration errors into subsequent quantitative reconstructions.

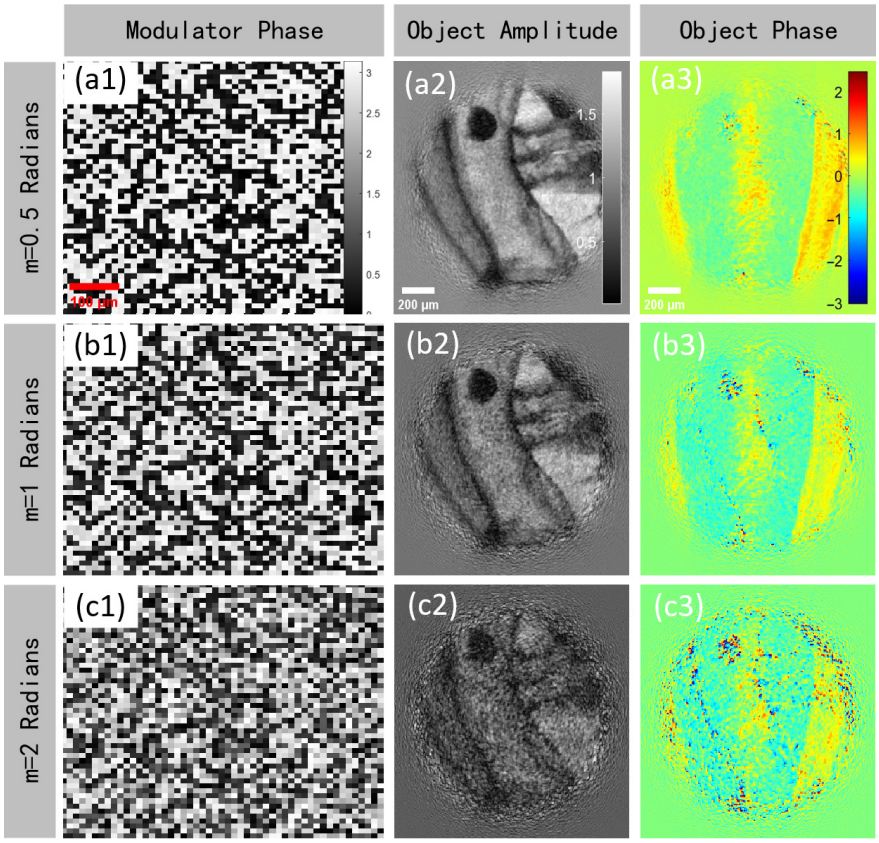


Figure 7. Reconstruction results of proposed method in the presence of modulator errors. (**a1**–**a3**) Modulator error with 0.5 radians and the corresponding reconstructed amplitude and phase; (**b1**–**b3**) Modulator error with 1 radians and the corresponding reconstructed amplitude and phase; (**c1**–**c3**) Modulator error with 2 radians and the corresponding reconstructed amplitude and phase.

Another critical factor influencing the proposed method is the optical propagation geometry. In actual experiments, the distance L between the CCD plane and the modulator phane, as well as the total distance $d_1 + d_2$ between the mdulator plane and aperture plane, are key parameters governing the forward model used in reconstruction. Small errors in measuring these distances (arising from mechanical misalignment) can introduce systematic phase mismatches that degrade reconstruction fidelity. To quantitatively evaluate their sensitivity, we performed two sets of controlled simulations. First, we isolated the effect

of error in L while holding $d_1 + d_2$ fixed at its nominal value (d_1 = 10 mm, d_2 = 20 mm, so $d_1 + d_2$ = 30 mm). The true value of L was set to 20 mm, in the reconstruction algorithm, L was deliberately mis-specified as 20.1 mm, 20.3 mm, and 20.5 mm, respectively. As shown in Figure 8(a1–a3), the method exhibits high sensitivity to L: at a deviation of only +0.3 mm, both amplitude contrast and phase continuity deteriorate markedly—fine features blur and background noise increases. Fortunately, L can be determined with high accuracy during the ptychographic characterization of the modulator itself, especially when employing an axial distance refinement scheme integrated into the ptychographic reconstruction loop [51]. Second, we assessed sensitivity to error in $d_1 + d_2$ while keeping L fixed at 20 mm. Here, d_1 remained constant at 10 mm, while d_2, whose nominal value is 20 mm, was mis-specified in reconstruction as 21 mm, 23 mm, and 25 mm. Figure 8(b1–b3) shows that increasing d_2 error induces progressive defocus-like blurring and diffraction-induced intensity ripples in the reconstructed amplitude, yet the global object outline and major phase gradients remain recognizable even at +5 mm. Crucially, this defocus artifact is physically consistent with a quadratic phase error and can therefore be effectively compensated using the autofocus algorithm introduced earlier, confirming that the method is inherently robust against moderate uncertainties in $d_1 + d_2$.

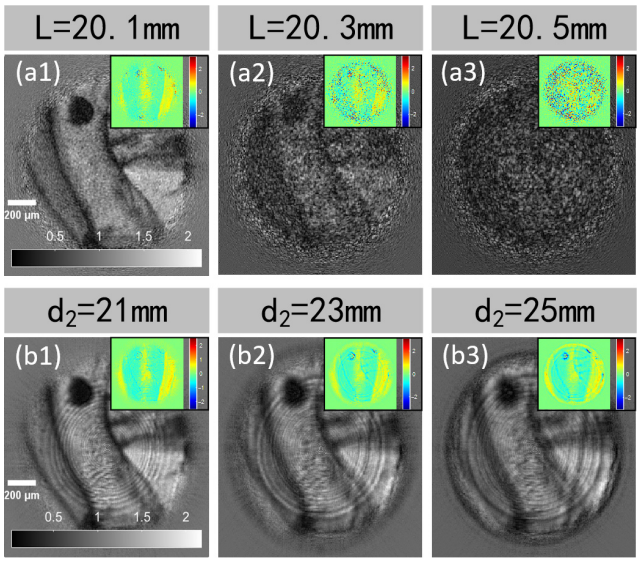


Figure 8. Reconstruction results of proposed method in the presence of propagation errors. (**a1**–**a3**) Reconstructed amplitude and phase with erroneous distance L set to be 20.1 mm, 20.3 mm, 20.5 mm, respectively; (**b1**–**b3**) recosntructed amplitude and phase with erroneous distance d_2 set to be 21 mm, 23 mm, 25 mm, respectively; the intsets are the corresponding reconstructed phase.

Since Equation (9) updates the probe function using an explicitly defined aperture, the geometric fidelity of this aperture, particularly its size and shape, directly influences the accuracy of the forward model, and thus impacts reconstruction quality. To systematically evaluate sensitivity to aperture size error, we conducted simulations in which the nominal aperture diameter was varied while keeping all other parameters fixed. The ground-truth aperture diameter was set to 200 pixels; in the reconstruction algorithm, it was deliberately mis-specified as 192, 196, 204, and 208 pixels (corresponding to relative errors of -4%, -2%, +2%, and +4%, respectively). As shown in Figure 9, the proposed method exhibits moderate sensitivity to aperture size: deviations beyond $\pm 2\%$ introduce visible diffraction rings in both the reconstructed amplitude and phase maps. In actual experiment, the circular aperture used to define the probe is not assumed a priori but is instead extracted directly from the ptychographically reconstructed probe function. Meanwhile, the triangular aperture used in reconstruction algorithm is the designed standard triangle.

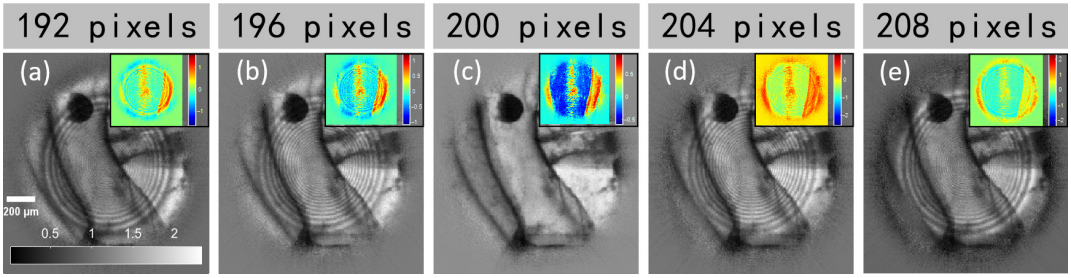


Figure 9. Reconstruction results of proposed method in the presence of aperture errors. (**a**–**e**) Reconstructed amplitude and phase with aperture size set to be 192 pixels, 196 pixels, 200 pixels, 204 pixels, 208 pixels, respectively; the intsets in (**a**–**e**) are the reconstructed phase.

Another critical source of error arises from the discrepancy between the actual incident wavefront at the aperture plane and the idealized plane wavefront assumed in Equation (9). Specifically, Equation (9) prescribes a perfectly normal-incident, spatially uniform illumination; however, real optical systems inevitably introduce wavefront aberrations, due to imperfect collimation, lens imperfections, or air turbulence. To quantify this effect, we performed a controlled simulation comparing two illumination conditions: (i) a complex illumination probe to simulate the actual situation, as shown in Figure 10a, and (ii) an ideal plane wave, as shown in Figure 10b. Both probes were propagated through identical system geometry (L = 20 mm, d_1 = 10 mm, d_2 = 20 mm) and processed using the identical reconstruction algorithm, the reconstructed results are shown in Figure 10c and d, respectively. As evident, the complex illumination induces strong, structured artifacts in both amplitude and phase. To isolate the multiplicative nature of this error, we computed the pixel-wise ratio of the real reconstruction (Figure 10c) to the ideal reconstruction (Figure 10d), yielding the correction map shown in Figure 10e. Back-propagating this map over distance d_1 yields the field at the aperture plane (Figure 10f), and we noted that this result was very similar with the complex illumination probe in Figure 10a. This confirms that the wavefront mismatch manifests as a deterministic, multiplicative perturbation on the reconstructed object function. In practice, experimental results demonstrate that such wavefront deviations do not compromise quantitative interpretation of object structure, confirming the method's tolerance to moderate illumination non-ideality.

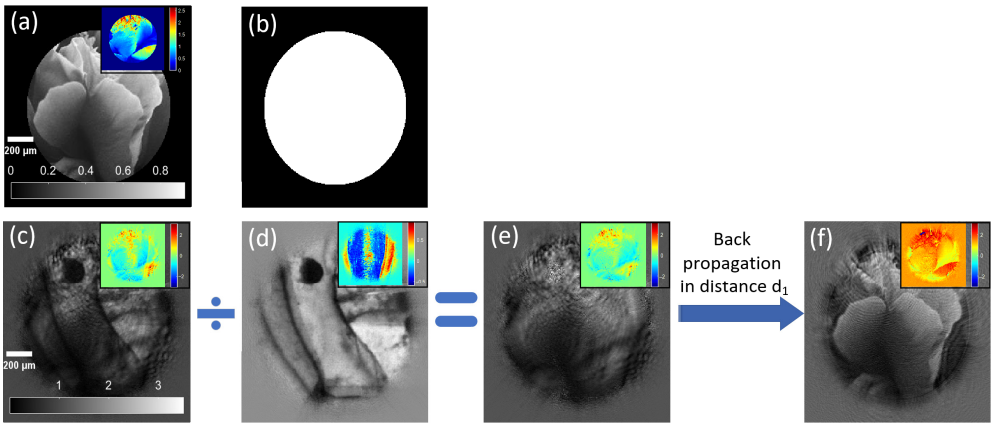


Figure 10. Analysis of the impact of illumination discrepancy on the reconstructed results. (**a**,**c**) Complex illumination probe at the aperture plane and the corresponding reconstructed amplitude and phase; (**b**,**d**) ideal plane wave at the aperture plane and the corresponding reconstructed amplitude and phase; (**e**) the result of dividing (**c**) by (**d**); (**f**) back propagating (**e**) in distance d_1; the intsets are the corresponding phases.

4. Experimental Demonstration

The proposed method was verified with experiments using visible light. In the experiment, a He–Ne laser light source with a wavelength of 632.8 nm was used. The laser beam passed through a spatial filter and a lens to form a plane-wave illumination. This plane wave was then passed through a polygon aperture. Both a circular aperture and triangular aperture with the same area were used in experiment; the diameter of the circular aperture was 2 mm, and the side length of the triangular aperture was 2.693 mm. A holographic diffuser plate with 1° angle of divergence was placed 85.94 mm downstream of the aperture plane as the phase plate modulator. This diffuser plate had a weak modulation effect and was mounted on an X–Y stage. The complex function of phase plate was measured in advance with ptychography, first, a circular aperture of 2 mm diameter was used to generate a planar wave illumination at the modulator plane. The phase plate modulator was then translated in a 10 × 10 raster scan with a nominal step size of 0.297 mm (a random offset of 0.0275 mm was added to each step). A CMOS camera (8-bit dynamic range, pixel pitch 5.5 μm, active resolution 2048 × 2048, made in Germany) was positioned precisely 98.3591 mm downstream of the modulator plane to record the diffraction patterns at all 100 scan positions. The acquired intensity measurements were subsequently fed into the extended ptychographic iterative engine (ePIE) algorithm [20] to reconstruct the complex transmission function of the modulator. During reconstruction, two complementary error-correction modules were integrated: (i) a lateral translation position error-correction algorithm [21] and (ii) an axial distance error-correction algorithm [51] were applied to improve the reconstruction quality, and the final reconstructed amplitude and phase maps of the modulator are shown in Figure 11.

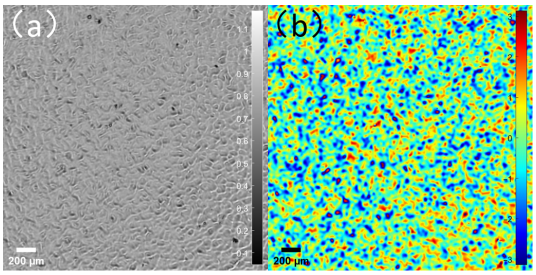


Figure 11. Reconstructed amplitude and phase of the phase modulator. (**a**) The reconstructed amplitude; (**b**) the reconstructed phase.

A USAF resolution target was selected as the tested object. The object was placed at three different axial positions (d_1 = 15, 25, and 35 mm). Subsequent to the autofocus algorithm correction, the three final corrected axial positions were determined to be 16.22, 25.5, 35.4 mm. After a single exposure by the camera, the intensity of the recorded diffraction pattern, the complex function of modulator, and the corrected distance, d_1, were incorporated into the proposed algorithm for 500 iterations. The same dataset was also used in the conventional CMI algorithm with the same parameters to reconstruct the pure object function with direct-division method; all the reconstructed results are shown in Figure 12.

The experimental results indicate that regardless of the position of the tested object, the proposed method can consistently reconstruct the pure object function with high fidelity. In contrast, the amplitudes reconstructed by the direct-division method appear darker and exhibit lower contrast, especially when the object distance d_1 becomes larger. These experimental results are in agreement with simulation. The experimental results reconstructed by the proposed method still have some artifacts in background because of the loss of the high frequency information in ptychography measurement, the discrepancy

between the real wavefront and the reconstructed plane wavefront at the aperture plane (as shown in Figure 13), and the estimated error of the practical aperture size in the iterative algorithm. It should be noted that the reconstruction quality using triangular aperture is lower than that using circular aperture. This is because the circular aperture used in reconstruction algorithm is reconstructed from ptychography results, which are more accurate, while the triangular aperture used in the reconstruction algorithm is a standard triangle. The line profile of reconstructed amplitude with circular aperture (Figure 12b) is shown in Figure 14. It can be seen that group 5 element 1 of this resolution target can be distinguished; the corresponding resolution is 15.63 μm.

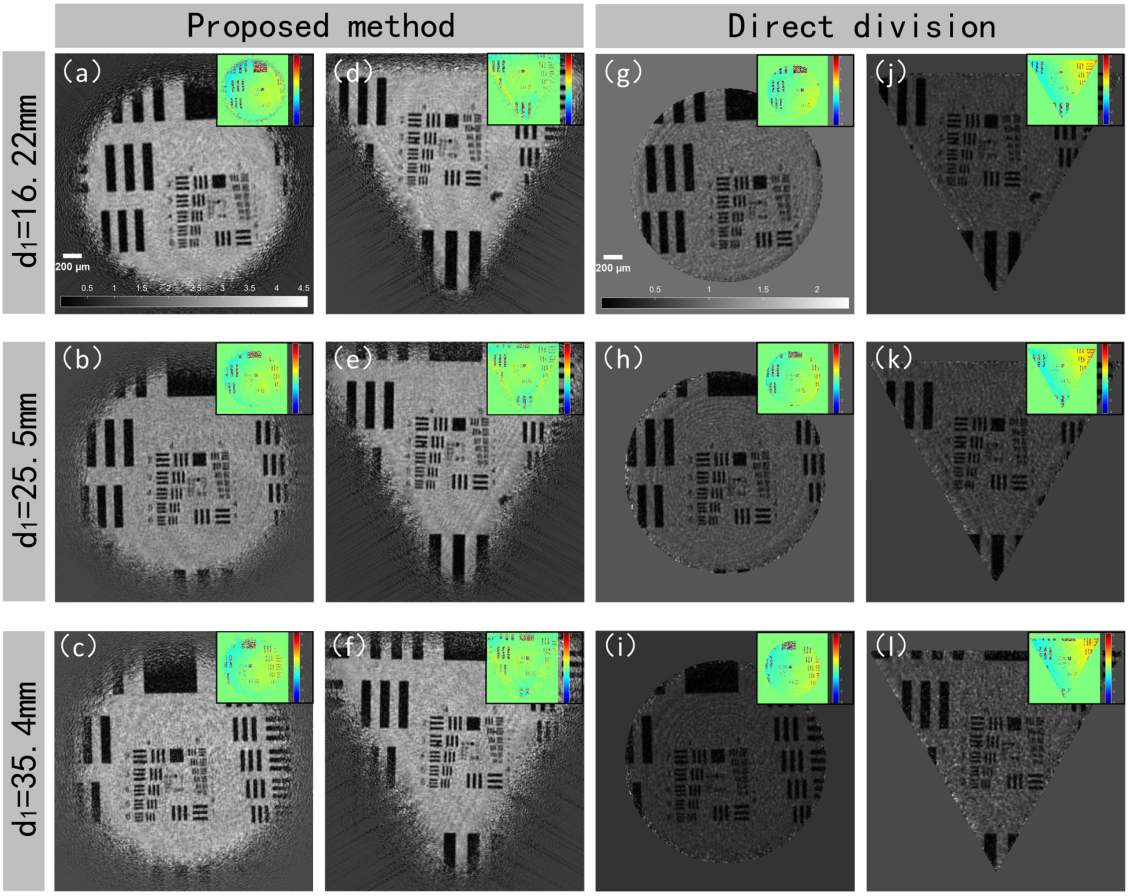


Figure 12. Experimental results. (**a**–**c**) The reconstructed amplitude and phase of pure object function at different distances by proposed method with circular aperture; (**d**–**f**) the reconstructed amplitude and phase of pure object function at different distances by proposed method with triangular aperture; (**g**–**i**) the reconstructed amplitude and phase of pure object function at different distances by direct divison method with circular aperture; (**j**–**l**) the reconstructed amplitude and phase of pure object function at different distances by direct-division method with triangular aperture; the intsets in (**a**–**l**) are the reconstructed phases.

To experimentally validate the phase recovery capability of the proposed method, a mixed phase-amplitude object (a bee wing) was selected as the measured sample, before placing this sample into the optical path, a diffraction pattern without sample was recorded by the detector. This diffraction pattern (without sample) was then added to the diffraction pattern obtained with the sample. As shown in Figure 15a, due to the uneven thickness of the sample, the diffraction pattern has shifted, resulting in a change in the illuminated area on the modulator plane. In this case, the eCMI method may not be applicable. However, the proposed method can retrieve the amplitude and phase of the sample, as demonstrated

in Figure 15b,c. Except some slight illumination artifacts, the reconstructed amplitude and phase exhibit clear and distinguishable outlines.

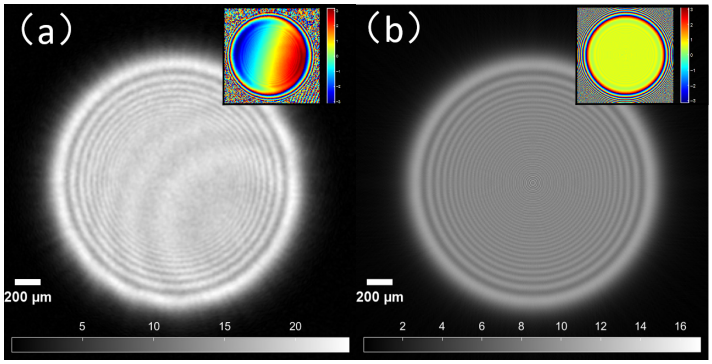


Figure 13. Reconstructed illuminating probe comparison. (**a**) The illuminating probe reconstructed by ptychography at distance $d_1 = 25.5$ mm; (**b**) the illuminating probe reconstructed by proposed method at the same distance; the intsets in (**a**,**b**) are the corresponding phases.

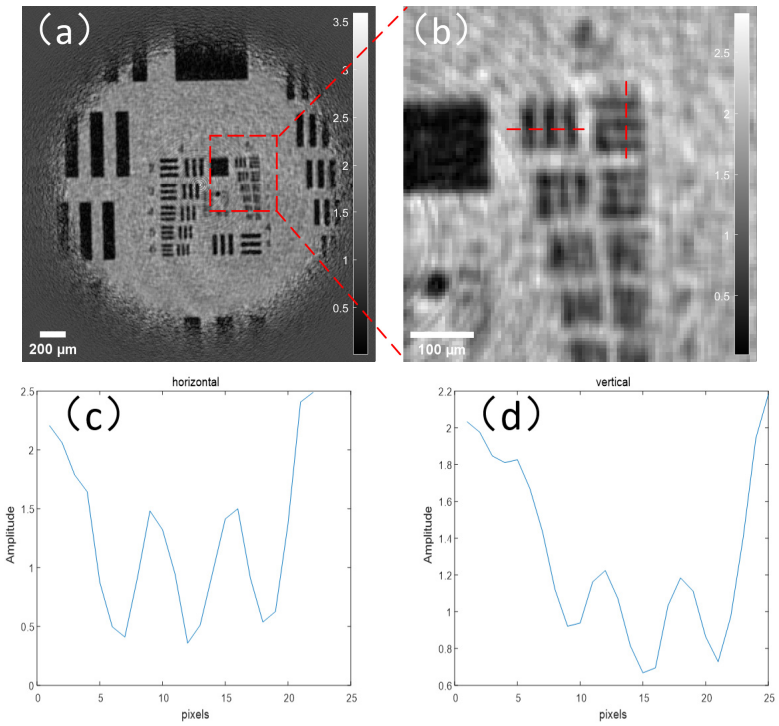


Figure 14. Resolution analysis of experimental results. (**a**) The reconstructed amplitude by proposed method at distance $d_1 = 25.5$ mm; (**b**) the enlarged version of the red dashed box in (**a**); (**c**) the horizontal line profile in (**b**); (**d**) the vertical line profile in (**b**).

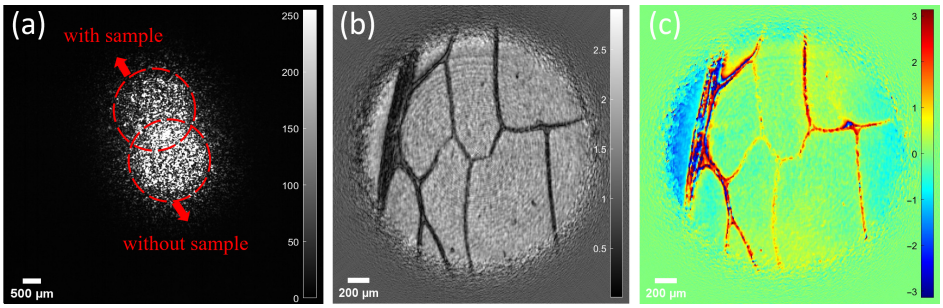


Figure 15. Diffraction patterns and reconstructed results of mixed phase-amplitude object. (**a**) Diffraction pattern superimposed when the sample is placed and when it is not placed. (**b**) Reconstructed amplitude of mixed phase-amplitude object. (**c**) Reconstructed phase of mixed phase-amplitude object.

5. Discussion

In the experimental demonstration, both circular and triangular apertures were used, and the reconstruction processes for these two apertures appear a little different. For the circular aperture, the reconstruction utilized an aperture function derived from the ptychography measurement of the modulator; this function was deduced via the back-propagation of the reconstructed probe function. In contrast, for the triangular aperture, an ideal standard triangle function was used. This is because we aim to present the best experimental results, while the real circular aperture function could be accurately incorporated, the actual triangular aperture function could not be retrieved from the ptychography results within our single diffraction pattern framework. Although the real triangular aperture function could be obtained using the conventional CMI method, doing so would violate the core principle of recording only one diffraction pattern. Therefore, an ideal standard triangle function was adopted for the triangular aperture reconstruction.

It is important to note that while the proposed method reconstructs the complex transmission function of the object using a single diffraction pattern, this approach entails significant trade-offs. In contrast, the eCMI method utilizes a diffraction pattern acquired without the sample to constrain the probe and modulator, thereby improving robustness against modulator errors. Removing this constraint can render the inverse problem more ill-posed. However, when imaging real mixed phase-amplitude objects, the diffraction patterns with and without the sample do not align at the detector plane (as shown in Figure 15a). This misalignment indicates that the illumination areas at the modulator plane differ between the two scenarios, rendering the eCMI method inapplicable. Under these circumstances, the proposed single-pattern method demonstrates distinct advantages. Although the reconstruction exhibits slight illumination artifacts due to discrepancies between the reconstructed and actual probes at the object plane, it remains a convenient and efficient tool for obtaining a highly approximate transmission function of the sample. Consequently, a key objective for future work is to improve the method to enable the precise, simultaneous reconstruction of both the illumination probe and the sample distribution from a single diffraction pattern.

Both numerical simulations and experimental results have demonstrated that the proposed method remains effective even under weak modulation conditions. This approach offers distinct advantages over the eCMI method, primarily because the requirements for the phase plate modulator are significantly relaxed. Specifically, the designed feature size and depth of the modulator can be larger and shallower, respectively. Consequently, phase modulators meeting these specifications are easier to fabricate, thereby enhancing the practical applicability and convenience of the proposed method.

6. Conclusions

In this work, a modified CMI algorithm for reconstructing the pure object function from a single diffraction pattern has been proposed. This method is highly independent of the object distance, and can work in weak modulation conditions, greatly relaxing the design requirements of the phase plate. This demonstrates a clear advantage over the conventional CMI and eCMI methods. The modulation effect of the phase plate, combined with an updated strategy at the object and the aperture planes, ensures the quality of the reconstruction results. In experiments, the more accurately the practical aperture shape is estimated, the better are the reconstruction results. Both simulation and experimental results have demonstrated the feasibility of the proposed method. It is believed that this method has strong potential for single-shot phase imaging and dynamic imaging applications.

https://doi.org/10.3390/photonics13040349

Author Contributions: Conceptualization, X.H.; methodology, Q.W.; software, Y.Z.; validation, Y.W. (Ye Wu); formal analysis, X.G.; investigation, X.L.; resources, W.Z.; data curation, X.H.; writing—original draft preparation, Y.W. (Yue Wang); writing—review and editing, X.H.; visualization, Y.Z.; supervision, W.Z.; project administration, X.H.; funding acquisition, L.J. All authors have read and agreed to the published version of the manuscript.

Funding: This research was funded by Innovative Training Program for College Students (DC2024019), Doctoral Scientific Research Foundation of Hubei University of Automotive Technology (BK202305), Open Fund of Shiyan Key Laboratory of Quantum Information and Precision Optics (SYZDK12025B03) and Natural Science Foundation of Hubei Province (2024AFD109).

Institutional Review Board Statement: Not applicable.

Informed Consent Statement: Not applicable.

Data Availability Statement: The data presented in this study are available on reasonable request from the corresponding author.

Conflicts of Interest: The authors declare no conflicts of interest.

Abbreviations

The following abbreviations are used in this manuscript:

CDI	Coherent diffraction imaging
CMI	Coherent modulation imaging

References

1. Hoppe, W.; Strube, G. Beugung in inhomogenen Primärstrahlenwellenfeld. II. Lichtoptische Analogieversuche zur Phasenmessung von Gitterinterferenzen. *Acta Crystallogr.* **1969**, *25*, 502–507. [CrossRef]
2. Fienup, J.R. Phase retrieval algorithms: A comparison. *Appl. Opt.* **1982**, *21*, 2758–2769. [CrossRef]
3. Miao, J.; Sayre, D.; Chapman, H.N. Phase retrieval from the magnitude of the Fourier transforms of nonperiodic objects. *J. Opt. Soc. Am. A* **1998**, *15*, 1662–1669. [CrossRef]
4. Nugent, K.A.; Peele, A.G.; Chapman, H.N.; Mancuso, A.P. Unique phase recovery for nonperiodic objects. *Phys. Rev. Lett.* **2003**, *91*, 203902. [CrossRef] [PubMed]
5. Itoh, H.; Nagai, K.; Sato, G.; Yamaguchi, K.; Nakamura, T.; Kondoh, T.; Ouchi, C.; Teshima, T.; Setomoto, Y.; Den, T. Two-dimensional grating-based X-ray phase-contrast imaging using Fourier transform phase retrieval. *Opt. Express* **2011**, *19*, 3339–3346. [CrossRef] [PubMed]
6. Xu, Y.; Pan, X.; Sun, M.; Liu, W.; Liu, C.; Zhu, J. single-shot ultrafast multiplexed coherent diffraction imaging. *Photonics Res.* **2022**, *10*, 1937–1946. [CrossRef]
7. Shapiro, D.; Thibault, P.; Beetz, T.; Elser, V.; Howells, M.; Jacobsen, C.; Kirz, J.; Lima, E.; Miao, H.; Neiman, A.M.; et al. Biological imaging by soft X-ray diffraction microscopy. *Proc. Natl. Acad. Sci. USA* **2005**, *102*, 15343–15346. [CrossRef]
8. Jiang, H.; Xu, R.; Chen, C.; Yang, W.; Fan, J.; Tao, X.; Song, C.; Kohmura, Y.; Xiao, T.; Wang, Y.; et al. Three-dimensional coherent X-ray diffraction imaging of molten iron in mantle olivine at Nanoscale resolution. *Phys. Rev. Lett.* **2013**, *110*, 205501. [CrossRef]
9. Jiang, H.; Song, C.; Chen, C.; Xu, R.; Raines, K.S.; Fahimian, B.P.; Lu, C.; Lee, T.; Nakashima, A.; Urano, J.; et al. Quantitative 3D imaging of whole, unstained cells by using X-ray diffraction microscopy. *Proc. Natl. Acad. Sci. USA* **2010**, *107*, 11234–11239. [CrossRef]
10. van der Schot, G.; Svenda, M.; Maia, F.; Hantke, M.; Deponte, D.; Seibert, M.; Aquila, A.; Schulz, J.; Kirian, R.; Liang, M.; et al. Imaging single cells in a beam of live cyanobacteria with an X-ray laser. *Nat. Commun.* **2015**, *6*, 5704. [CrossRef]
11. Chapman, H.; Nugent, K. Coherent lensless X-ray imaging. *Nat. Photonics* **2010**, *4*, 833–839. [CrossRef]
12. Miao, J.; Ishikawa, T.; Robinson, I.K.; Murnane, M.M. Beyond crystallography: Diffractive imaging using coherent X-ray light sources. *Science* **2015**, *348*, 530–535. [CrossRef] [PubMed]
13. Shahmoradian, S.H.; Tsai, E.H.R.; Diaz, A.; Guizar-Sicairos, M.; Raabe, J.; Spycher, L.; Britschgi, M.; Ruf, A.; Stahlberg, H.; Holler, M. Three-dimensional imaging of biological tissue by cryo X-ray ptychography. *Sci. Rep.* **2017**, *7*, 6291. [CrossRef] [PubMed]
14. Hue, F.; Rodenburg, J.M.; Maiden, A.M.; Sweeney, F.; Midgley, P.A. wave-front phase retrieval in transmission electron microscopy via ptychography. *Phys. Rev. B* **2010**, *82*, 121415. [CrossRef]

15. Carlino, E.; Scattarella, F.; De Caro, L.; Giannini, C.; Siliqi, D.; Colombo, A.; Galli, D.E. Coherent diffraction imaging in transmission electron microscopy for atomic resolution quantitative studies of the matter. *Materials* **2018**, *11*, 2323. [CrossRef]
16. Zuo, J.M.; Vartanyants, I.; Gao, M.; Zhang, R.; Nagahara, L.A. Atomic resolution imaging of a carbon nanotube from diffraction intensities. *Science* **2003**, *300*, 1419–1421. [CrossRef] [PubMed]
17. Guizar-Sicairos, M.; Fienup, J.R. Understanding the twin-image problem in phase retrieval. *J. Opt. Soc. Am. A* **2012**, *29*, 2367–2375. [CrossRef]
18. Fienup, J.R.; Wackerman, C.C. Phase-retrieval stagnation problems and solutions. *J. Opt. Soc. Am. A* **1986**, *3*, 1897–1907. [CrossRef]
19. Rodenburg, J.M.; Faulkner, H.M.L. A phase retrieval algorithm for shifting illumination. *Appl. Phys. Lett.* **2004**, *85*, 4795–4797. [CrossRef]
20. Maiden, A.M.; Rodenburg, J.M. An improved ptychographical phase retrieval algorithm for diffractive imaging. *Ultramicroscopy* **2009**, *109*, 1256–1262. [CrossRef]
21. Zhang, F.; Peterson, I.; Vila-Comamala, J.; Diaz, A.; Berenguer, F.; Bean, R.; Chen, B.; Menzel, A.; Robinson, I.K.; Rodenburg, J.M. Translation position determination in ptychographic coherent diffraction imaging. *Opt. Express* **2013**, *21*, 13592–13606. [CrossRef]
22. Xu, W.; Lin, H.; Wang, H.; Zhang, F. Super-resolution near-field ptychography. *Opt. Express* **2020**, *28*, 5164–5178. [CrossRef]
23. Pan, X.; Liu, C.; Lin, Q.; Zhu, J. Ptychographic iterative engine with self-positioned scanning illumination. *Opt. Express* **2013**, *21*, 6162–6168. [CrossRef]
24. Sidorenko, P.; Cohen, O. Single-shot ptychography. *Optica* **2016**, *3*, 9–14. [CrossRef]
25. Pan, X.; Liu, C.; Zhu, J. Single shot ptychographical iterative engine based on multi-beam illumination. *Appl. Phys. Lett.* **2013**, *103*, 171105. [CrossRef]
26. Zhang, F.; Rodenburg, J.M. Phase retrieval based on wave-front relay and modulation. *Phys. Rev. B* **2010**, *82*, 121104. [CrossRef]
27. Zhang, F.; Chen, B.; Morrison, G.R.; Vila-Comamala, J.; Guizar-Sicairos, M.; Robinson, I.K. Phase retrieval by coherent modulation imaging. *Nat. Commun.* **2016**, *7*, 13367. [CrossRef]
28. Pan, X.; Liu, C.; Zhu, J. Iterative convergence and reconstruction uniqueness of coherent modulation imaging. *Acta Opt. Sin.* **2020**, *40*, 1811001. [CrossRef]
29. He, X.; Tao, H.; Pan, X.; Liu, C.; Zhu, J. High-quality laser beam diagnostics using modified coherent phase modulation imaging. *Opt. Express* **2018**, *26*, 6239–6248. [CrossRef] [PubMed]
30. Yi, J.; Zhao, J.; Wang, B.; Wang, Y.; Zhang, F. Surface metrology by multiple-wavelength coherent modulation imaging. *Appl. Opt.* **2022**, *61*, 7218–7224. [CrossRef]
31. Zhang, F.; Pedrini, G.; Osten, W. Phase retrieval of arbitrary complex-valued fields through aperture-plane modulation. *Phys. Rev. A* **2007**, *75*, 043805. [CrossRef]
32. Dong, X.; Pan, X.; Liu, C.; Zhu, J. Single shot mutli-wavelength phase retrieval with coherent modulation imaging. *Opt. Lett.* **2018**, *43*, 1762–1765. [CrossRef]
33. Zhang, J.; Yang, D.; Tao, Y. Spatiotemporal coherent modulation imaging for dynamic quantitative phase and amplitude microscopy. *Opt. Express* **2021**, *29*, 38451–38464. [CrossRef]
34. Pan, X.; Liu, C.; Zhu, J. Coherent amplitude modulation imaging based on partially saturated diffraction pattern. *Opt. Express* **2018**, *26*, 21929–21938. [CrossRef] [PubMed]
35. Pan, X.; Veetil, S.P.; Liu, C.; Tao, H.; Jiang, Y.; Lin, Q.; Li, X.; Zhu, J. On-shot laser beam diagnostics for high-power laser facility with phase modulation imaging. *Laser Phys. Lett.* **2016**, *13*, 055001. [CrossRef]
36. Zhang, J.; Yang, D.; Lv, W.; Jin, X.; Shi, Y. Three-dimensional phase and intensity reconstruction from coherent modulation imaging measurements. *Opt. Express* **2022**, *30*, 20415–20430. [CrossRef]
37. Pan, X.; Liu, C.; Zhu, J. Phase retrieval with extended field of view based on continuous phase modulation. *Ultramicroscopy* **2019**, *204*, 10–17. [CrossRef]
38. Wang, B.; Wang, Q.; Lyu, W.; Zhang, F. Modulator refinement algorithm for coherent modulation imaging. *Ultramicroscopy* **2020**, *216*, 113034. [CrossRef]
39. Wang, B.; He, Z.; Zhang, F. Coherent modulation imaging using unknown modulators. *Opt. Express* **2021**, *29*, 30035–30044. [CrossRef] [PubMed]
40. Zhao, J.; Xu, W.; Yi, J.; Wang, B.; Zhang, F. Extended coherent modulation imaging for single-shot object retrieval free from illumination artifacts. *Ultramicroscopy* **2022**, *240*, 113591. [CrossRef]
41. Gao, Y.; Zhang, J.; Yang, D.; Lyu, W.; Ruan, T.; Shi, Y. Blind coherent modulation imaging using momentum acceleration and sample priors. *J. Opt.* **2024**, *26*, 065603. [CrossRef]
42. Geng, Y.; Wen, X.; Tan, J.; Liu, S.; Liu, Z. Noise-robust phase retrieval by optics path modulation with adaptive feedback. *Opt. Commun.* **2022**, *515*, 128199. [CrossRef]
43. Williams, G.J.; Quiney, H.M.; Dhal, B.B.; Tran, C.Q.; Nugent, K.A.; Peele, A.G.; Paterson, D.; de Jonge, M.D. Fresnel coherent diffractive imaging. *Phys. Rev. Lett.* **2006**, *97*, 025506. [CrossRef] [PubMed]

44. Levitan, A.L.; Keskinbora, K.; Sanli, U.T.; Weigand, M.; Comin, R. Single-frame far-field diffractive imaging with randomized illumination. *Opt. Express* **2020**, *28*, 37103–37116. [CrossRef] [PubMed]
45. Levitan, A.L.; Keskinbora, K.; Pancaldi, M.; Dieter Engel, W.; Pedersoli, E.; Capotondi, F.; Comin, R. Single-shot imaging with randomized structured illumination at a free electron laser. *Opt. Express* **2026**, *34*, 8043–8052. [CrossRef]
46. Chew, S.H.; Eschen, W.; Liu, C.; Abdelaal, M.; Limpert, J.; Rothhardt, J. Single-frame randomized probe imaging in the EUV using a high-order harmonic source. *Opt. Express* **2026**, *34*, 7496–7508. [CrossRef] [PubMed]
47. Kang, J.; Takazawa, S.; Ishiguro, N.; Takahashi, Y. Single-frame coherent diffraction imaging of extended objects using triangular aperture. *Opt. Express* **2021**, *29*, 1441–1453. [CrossRef]
48. Brames, B.J. Unique phase retrieval with explicit support information. *Opt. Lett.* **1986**, *11*, 61–63. [CrossRef]
49. Dou, J.; Gao, Z.; Ma, J.; Yuan, C.; Yang, Z.; Wang, L. Iterative autofocusing strategy for axial distance error correction in ptychography. *Opt. Lasers Eng.* **2017**, *98*, 56–61. [CrossRef]
50. Wang, L.; Dou, J.; Ma, J.; Yuan, C.; Gao, Z.; Wei, C.; Zhang, T. Detection of the binary optical element based on ptychography. *Acta Phys. Sin.* **2017**, *66*, 094201. [CrossRef]
51. Ruan, T.; Lv, W.; Tao, Y.; Zhang, J.; Yan, X.; Yang, D.; Shi, Y. Adaptive total variation based autofocusing strategy in ptychography. *Opt. Lasers Eng.* **2022**, *158*, 107136. [CrossRef]

Disclaimer/Publisher's Note: The statements, opinions and data contained in all publications are solely those of the individual author(s) and contributor(s) and not of MDPI and/or the editor(s). MDPI and/or the editor(s) disclaim responsibility for any injury to people or property resulting from any ideas, methods, instructions or products referred to in the content.